Attenuated cerebellar phenotypes in *Inpp4a* truncation mutants with preserved phosphatase activity

Dang Minh Tran[1], Nozomu Yoshioka[1], Norihisa Bizen[1], Yukiko Mori-Ochiai[1], Masato Yano[1], Shogo Yanai[2], Junya Hasegawa[2], Satoshi Miyashita[3], Mikio Hoshino[3], Junko Sasaki[2], Takehiko Sasaki[2], and Hirohide Takebayashi[1,4]

[1]Division of Neurobiology and Anatomy, Graduate School of Medical and Dental Sciences, Niigata University, Niigata, Japan.

[2]Department of Biochemical Pathophysiology, Medical Research Institute, Tokyo Medical and Dental University (TMDU), Tokyo Japan.

[3]Department of Biochemistry and Cellular Biology, National Institute of Neuroscience, National Center of Neurology and Psychiatry (NCNP), Tokyo, Japan.

[4]Center for Coordination of Research Facilities (CCRF), Niigata University, Niigata, Japan.

Present address of SM: Department of System Pathology for Neurological Disorders, Brain Research Institute, Niigata University, Niigata, Japan.

*Address correspondence to: Hirohide Takebayashi, Division of Neurobiology and Anatomy, Graduate School of Medical and Dental Sciences, 1-757 Asahimachi-dori, Niigata 951-8510, Japan. Phone: 81.25.227.2053; E-mail: takebaya@med.niigata-u.ac.jp.

Keywords: Phosphoinositide (PIP), cerebellar atrophy, inositol polyphosphate-4-phosphatase type I (Inpp4a), pain-induced epilepsy, neurodegeneration, mouse model

Conflict of interest

The authors have declared that no conflict of interest exists.

Abstract

Phosphoinositides (PIPs) act as intracellular signaling molecules that regulate various cellular processes. Abnormalities in PIP metabolism cause various pathological conditions, including neurodegenerative diseases, cancer, and immune disorders. Several neurological diseases with diverse phenotypes, such as ataxia with cerebellar atrophy or intellectual disability without brain malformation, are caused by mutations in *INPP4A*, which encodes a phosphoinositide phosphatase. This study examined two strains of *Inpp4a* mutant mice with distinct cerebellar phenotypes: the first *Inpp4a*$^{\Delta Ex1,2}$ mutant exhibited striatal degeneration without cerebellar atrophy, and the other *Inpp4a*$^{\Delta Ex23}$ mutant exhibited a severe striatal phenotype with cerebellar atrophy. Both strains exhibited reduced expressions of Inpp4a mutant proteins in the cerebellum. N-terminal truncated Inpp4a proteins were expressed from *Inpp4a*$^{\Delta Ex1,2}$ allele by alternative translation initiation and had phosphatase activity for PI(3,4)P_2, whereas the Inpp4a mutant protein encoded by *Inpp4a*$^{\Delta Ex23}$ completely lacked phosphatase activity. The diverse phenotypes observed in *Inpp4a*-related neurological diseases could be due to the varying protein expression levels and retained phosphatase activity in different Inpp4a variants. These findings provide insights into the role of Inpp4a mutations in disease pathogenesis and may help to develop personalized therapy.

Introduction

Phosphoinositides (PIPs) are phosphorylated forms of phosphatidylinositol that are present at relatively low levels within cells. These are unique phospholipids because they can be modified rapidly by headgroup phosphorylation/dephosphorylation by dozens of kinases and phosphatases to transiently generate (or remove) membrane-targeting signals at particular intracellular locations (Balla, 2013; Sasaki et al., 2009). PIPs regulate various cellular processes, including cytoskeletal remodeling, membrane trafficking, and ion channel activity (Echard, 2012; Nilius et al., 2008; Roth, 2004; Zolles et al., 2006). Abnormal metabolism of PIPs is involved in various physiological and pathological conditions, including developmental defects (Wu et al., 2020), cancer (Bunney and Katan, 2010), neurological disease (Volpatti et al., 2019; Waugh, 2015), and immune disorders (Aich et al., 2012; Nigorikawa et al., 2015).

INPP4A catalyzes the removal of the 4′-phosphate of phosphatidylinositol 3,4-bisphosphate [$PI(3,4)P_2$] and phosphatidylinositol 3,4,5-trisphosphate [$PI(3,4,5)P_3$]. $PI(3,4)P_2$ is a phosphoinositide 3-kinase-generated lipid second messenger. INPP4A is widely and highly expressed in the brain, heart, and skeletal muscle (Norris et al., 1995). Ligand binding to growth factor receptors, such as Trk receptors, activates phosphoinositide 3-kinase, which then generates $PI(3,4,5)P_3$ from $PI(4,5)P_2$ (Vanhaesebroeck et al., 2010). Subsequently, SHIP1 and SHIP2 (also known as INPP5D and INPPL1, respectively) generate $PI(3,4)P_2$ from $PI(3,4,5)P_3$ (Hawkins and Stephens, 2016). $PI(3,4)P_2$ regulates neurite and dendrite development, and the phosphoinositide metabolism of $PI(3,4)P_2$ is crucial for neuronal development and the proper function of synapses in the nervous system (Zhang et al., 2017). Additionally, some PIPs metabolism enzyme genes are tumor suppressor genes, such as Phosphatase and tensin homologue (*PTEN*) and *INPP4B*. PTEN catalyzes removal of the 3′-phosphate of $PI(3,4)P_2$ and $PI(3,4,5)P_3$ (Fukumoto et al., 2017), and the N-terminal domain of PTEN binds to PIP_2 (Rahdar

et al., 2009). INPP4B is involved in DNA repair (Sun et al., 2020) and is a potential biomarker for the resistance of cancer cells to radiotherapy (Kim et al., 2012). Spontaneous mutation of the *Inpp4a* gene in *weeble* mutant mice results in postnatal cerebellar and striatal neuronal degeneration (Nystuen et al., 2001). Neurodegeneration in the striatum of *Inpp4a* knockout (KO) mice lacking the first and second coding exons (exons 1 and 2) was caused by excitotoxicity (Sasaki et al., 2010). Recent reports have demonstrated human diseases associated with *INPP4A* mutations (MIM: 600916) (Banihashemi et al., 2020; Hecher et al., 2023; Najmabadi et al., 2011; Özkan Kart et al., 2023; Sheffer et al., 2015); However, different mutations result in different disease phenotypes. A nonsense mutation, c.115 C > T p.Gln39X, in the conserved N-terminal domain of INPP4A, leads to intellectual disability without brain malformation (Banihashemi et al., 2020), while homozygous genomic deletion of 1770 bp within the *INPP4A* gene causes myoclonic epilepsy, microcephaly, and atrophy of the cerebellum (Sheffer et al., 2015). Although there is diversity in the neuropathological phenotypes caused by different *INPP4A* mutations, the underlying molecular mechanisms are unknown.

To understand the heterogeneous brain phenotypes of *Inpp4a* mutants, we examined two strains of *Inpp4a* mutant mice that exhibit different phenotypes. One strain has cerebellar atrophy, and the other does not. *Inpp4a* mutants lacking exons 1 and 2 (*Inpp4a*$^{\Delta Ex1,2}$ KO mice) exhibited striatal degeneration but an intact cerebellum. In contrast, *Inpp4a* mutants lacking exon 23, which encodes a C-terminal phosphatase domain (*Inpp4a*$^{\Delta Ex23}$ KO mice), exhibited striatal degeneration and cerebellar atrophy. We demonstrate that the N-terminal truncated Inpp4a protein expressed in *Inpp4a*$^{\Delta Ex1,2}$ KO mice has phosphatase activity, which may account for the attenuated cerebellar phenotypes in the *Inpp4a*$^{\Delta Ex1,2}$ KO mice and phenotypic diversity of the *Inpp4a* mutant phenotypes.

Results

Diversity of cerebellar phenotypes in the two Inpp4a KO mouse lines.

Inpp4a$^{\Delta ex1,2}$ KO mice exhibited severely disordered involuntary movement, including limb hyperkinesia, opisthotonos, and dystonia (Movie 1) (Sasaki et al., 2010). *Inpp4a*$^{\Delta ex23}$ KO mice showed cerebellar atrophy and ataxic gait (Movie 2), similar to *weeble* mice (Nystuen et al., 2001). In contrast, the cerebellum in *Inpp4a*$^{\Delta Ex1,2}$ KO mice was of standard size compared with a relatively small cerebellum in *Inpp4a*$^{\Delta ex23}$ KO mice (Supplemental Fig. 1A, D). The brain and body weights of the *Inpp4a* mutants were smaller than those of wild-type mice (Supplemental Fig. 1B, C, E, F). Histological analysis confirmed that wild-type and *Inpp4a*$^{\Delta ex1,2}$ KO cerebella were of indistinguishable size (Fig. 1A, B), while the *Inpp4a*$^{\Delta ex23}$ KO cerebellum showed apparent atrophy (Fig. 1C). *Inpp4a*$^{\Delta ex23}$ KO mice exhibited both Purkinje cell loss (Fig. 1F) and activation of microglia (Fig. 1I), which were not present in *Inpp4a*$^{\Delta ex1,2}$ KO or wild-type mice (Fig. 1D, E, G, H). In addition, *Inpp4a*$^{\Delta ex1,2}$ KO mice exhibited pain-induced epilepsy (Movie 3), while *Inpp4a*$^{\Delta ex23}$ KO mice did not. These data indicate phenotypic diversity in the cerebellum between *Inpp4a*$^{\Delta ex1,2}$ and *Inpp4a*$^{\Delta ex23}$ KO mice. Purkinje cell degeneration was observed in the *Inpp4a*$^{\Delta ex23}$ KO cerebellum at the postnatal stage (Supplemental Fig. 2) as previously reported in weeble mice (Nystuen et al., 2001). Next, we performed immunohistochemistry using antibodies against the apoptotic markers, cleaved-Capase3 (cl-Casp3), and single-strand DNA (ssDNA). There was a remarkable upregulation of cl-Casp3 and ssDNA signals in the cerebellum of *Inpp4a*$^{\Delta ex23}$ KO mice but not of *Inpp4a*$^{\Delta ex1,2}$ KO mice (Fig. 2A–H). The apoptotic cells were mainly in the granule cell layer of the cerebellum at postnatal day 7 (P7) (Fig. 2C, F), and cl-Casp3-positive Purkinje cells were present in the *Inpp4a*$^{\Delta ex23}$ KO cerebellum (Fig. 2C). Despite the almost intact cerebellum in *Inpp4a*$^{\Delta ex1,2}$ mice, neurodegeneration was present in the striatum (Sasaki et al., 2010). We also confirmed

activation of microglia and astrocytes in the striatum of both *Inpp4a*$^{\Delta ex1,2}$ and *Inpp4a*$^{\Delta ex23}$ KO mice (Supplemental Fig. 3A–G), with the activation being more severe in *Inpp4a*$^{\Delta ex23}$ KO mice (Supplemental Fig. 3H).

Alternative exon use of Inpp4a transcripts in the cerebellum.

We performed *in situ* hybridization to investigate *Inpp4a* expression in wild-type and the two lines of *Inpp4a* KO mice. In wild-type mice, *Inpp4a* was widely expressed throughout the brain and cerebellum with very high levels in Purkinje cells (Fig. 3A) (Nystuen et al., 2001). *Inpp4a* mRNA was also detected in the brain of *Inpp4a*$^{\Delta ex1,2}$ and *Inpp4a*$^{\Delta ex23}$ KO mice (Fig. 3B, C); however, quantitative PCR (qPCR) data indicated a significant decrease in the level of *Inpp4a* mRNA compared with the wild type (Fig. 3D, E). Next, we examined the expression of Inpp4a protein in each area of the wild-type central nervous system by western blotting and detected two isoforms only in the cerebellum (Fig. 3F). We also investigated the expression of Inpp4a protein in the forebrain and cerebellum of wild-type, *Inpp4a*$^{\Delta ex1,2}$ KO, and *Inpp4a*$^{\Delta ex23}$ KO mice (Fig. 3G). As expected from the reduced mRNA levels, we observed dramatically reduced levels of mutant Inpp4a protein in the forebrain and cerebellum of both *Inpp4a*$^{\Delta ex1,2}$ KO and *Inpp4a*$^{\Delta ex23}$ KO mice (Fig. 3G). We observed faint band in *Inpp4a*$^{\Delta ex1,2}$ KO and *Inpp4a*$^{\Delta ex23}$ KO mice (Fig. 3G). We further confirmed the Inpp4a signals in the Purkinje cells of wild-type, *Inpp4a*$^{\Delta ex1,2}$ KO and *Inpp4a*$^{\Delta ex23}$ KO mice using immunohistochemistry (Supplemental Fig. 4).

The phosphatase domain of *Inpp4a* is encoded by exon 23, and several *Inpp4a* isoforms are generated by alternative splicing or distinct promoter use (Supplemental Fig. 5) (Shearn et al., 2001). We detected at least two isoforms in the wild-type cerebellum; therefore, we performed RNA-seq on the wild-type forebrain and cerebellum at two weeks of age. The RNA-seq analysis revealed alternative use of the exon encoding the C-terminal region by the forebrain and cerebellum (Fig. 4A). A previous study reported that alternative inclusion of exon 24 or exon 25 in the C-terminal region of *Inpp4a* generates *Inpp4a beta* and *Inpp4a alpha* isoforms,

respectively (Norris et al., 1997). Therefore, we performed qPCR to detect *Inpp4a beta* (Ex24), *Inpp4a alpha* (Ex25), and both *Inpp4a* (Ex22) (Fig. 4B–D). The *Inpp4a beta* isoform was highly expressed in the cerebellum (Fig. 4B), while the *Inpp4a alpha* isoform is expressed at a similar level between forebrain and cerebellum (Fig. 4C). These data are consistent to relatively high expression of total *Inpp4a* transcript in the cerebellum compared to the forebrain (Fig. 4D). Thus, stop codon of the *Inpp4a beta* isoform and *Inpp4a alpha* isoform are encoded by exon24 and exon25, respectively (Fig. 4E). The Inpp4a alpha isoform is expressed in the forebrain and cerebellum, while Inpp4a beta isoform is expressed only in the cerebellum. The Inpp4a beta isoform contains a putative transmembrane domain (Fig. 4F). Furthermore, RNA-seq data showed that exon 16 of *Inpp4a* is often excluded in the cerebellum (Fig. 4A). These data indicate that the cerebellum expresses unique *Inpp4a* isoforms compared with the forebrain. The lower and higher molecular weight isoforms in the cerebellum (Fig. 3) seem to correspond to *Inpp4a alpha* and *Inpp4a beta*, respectively.

Phosphatase activity of N-terminal truncated Inpp4a.

To investigate phosphatase activity of the Inpp4a proteins expressed from wild-type, $Inpp4a^{\Delta Ex1,2}$, and $Inpp4a^{\Delta Ex23}$ alleles towards PtdIns(3,4)P_2, we constructed a series of plasmids expressing FLAG-tagged Inpp4a proteins (pDNA3-Inpp4a-FLAG, a cerebellar isoform pcDNA3-Inpp4a CB-FLAG, pcDNA3-Inpp4a ΔEx1,2-FLAG, and pcDNA3-Inpp4a ΔEx23-FLAG). After transfection of HEK293T cells with these plasmids, we confirmed the production of the proteins by western blotting using a FLAG antibody (Fig. 5A). Notably, the level of Inpp4a CB-FLAG in the transfected cells was lower than that of the other Inpp4a-FLAG proteins. We then assessed the phosphatase activity of purified Inpp4a-FLAG proteins towards PtdIns(3,4)P_2 (Fig. 5B) by phosphoinositide regioisomer measurement using chiral column chromatography and mass spectrometry. Inpp4a has a phosphatase domain located in exon 23; therefore, as expected, Inpp4a ΔEx23-FLAG showed a loss of phosphatase activity compared

with the wild type (Fig. 5C). In contrast, Inpp4a ΔEx1,2-FLAG showed only a slight reduction of phosphatase activity (Fig. 5C). Therefore, the retention of phosphatase activity by the N-terminal truncated protein may be the main reason for the intact cerebellar phenotype in *Inpp4a*$^{\Delta Ex1,2}$ KO mice. Interestingly, a cerebellar Inpp4a isoform (Inpp4a CB-FLAG) had no phosphatase activity towards PtdIns(3,4)P_2. This result is consistent with a previous report showing the lack of phosphatase activity of the Inpp4a beta isoform expressed in insect cells (Yang et al., 2015). We also examined the intracellular localization of Inpp4a proteins by immunocytochemistry using a FLAG antibody (Fig. 5D). After transfection into NIH3T3 cells, only Inpp4a ΔEx1,2-FLAG showed altered localization in aggregation-like structures, indicating that the N-terminal C2 domain, which binds to PIPs, is essential for proper intracellular localization of Inpp4a.

Intracellular signaling is altered in Inpp4a-deficient cells.

Inpp4a deficiency results in activation of the Akt pathway through increased levels of PI(3,4)P_2 (Aich et al., 2012); therefore, we performed immunohistochemistry in the P21 brain using a well-established phospho-Akt antibody. We detected an upregulated phospho-Akt signal in the degenerating axons of *Inpp4a*$^{\Delta Ex23}$ KO Purkinje cells (Fig. 6C) but not in those of wild-type or *Inpp4a*$^{\Delta Ex1,2}$ KO mice (Fig. 6A, B). The Akt pathway is involved in axon degeneration (Yang et al., 2015); therefore, the Akt activation may be involved in the degeneration of Purkinje cell axons in the *Inpp4a*$^{\Delta Ex23}$ KO cerebellum.

Conditional knockout of Inpp4a in the mouse cerebellum.

To elucidate the function of Inpp4a in the cerebellum, we generated *En1-Cre*;*Inpp4a* conditional KO (cKO) mice. In *En1-Cre* knockin mice, Cre recombinase is expressed in cells that express engrailed 1 during embryonic development in the cerebellum and midbrain (Kimmel et al., 2000), resulting in the deletion of *Inpp4a* from the mesencephalon and

rhombomere 1-derived tissues including the cerebellum. To obtain *En1-Cre;Inpp4a* cKO (*En1-Cre;Inpp4a*$^{flox/flox}$) mice, we crossed female *Inpp4a*$^{flox/flox}$ mice with male *En1-Cre;Inpp4*$^{flox/+}$.

En1-Cre;*Inpp4a* cKO mice exhibited ataxia and a lifespan of only 4–5 weeks (Fig. 7A, Movie 4). Histological analyses showed severe atrophy of the cerebellum but not of other brain regions at three weeks old (Fig. 7B, C). In addition, Calbindin and Iba1 immunohistochemistry indicated apparent Purkinje cell loss (Fig. 7D, E) and activated microglia (Fig. 7F, G) in the cerebellum, respectively. In contrast, Iba1 immunohistochemistry in the striatum was similar between control and *En1-Cre*;*Inpp4a* cKO mice, indicating an intact striatum (Fig. 7H, I). These behavioral and histological defects are similar to those of *Inpp4a*$^{\Delta Ex23}$ KO mice, indicating that disruption of *Inpp4a* in the cerebellum is the leading cause of cerebellar atrophy and movement disorder in *Inpp4a*$^{\Delta Ex23}$ KO mice.

Discussion

We have investigated two lines of *Inpp4a* mutant mice side-by-side, and we report their phenotypic diversity here. Specifically, while striatal degeneration occurred in both *Inpp4a*$^{\Delta Ex23}$ and *Inpp4a*$^{\Delta Ex1,2}$ mutant lines, cerebellar degeneration was observed only in *Inpp4a*$^{\Delta Ex23}$ KO mice. Conversely, pain-induced epilepsy was observed only in *Inpp4a*$^{\Delta Ex1,2}$ KO mice. This is the first report on the attenuated cerebellar phenotypes and pain-induced epilepsy in the *Inpp4a*$^{\Delta Ex1,2}$ KO mice. Furthermore, we analyzed the properties of the *Inpp4a* transcripts and proteins from each mutant allele regarding exon composition and phosphatase activity. We found the expression of a previously unknown N-terminal truncated Inpp4a isoform in the cerebellum of *Inpp4a*$^{\Delta Ex1,2}$ KO mice. This isoform was produced by alternative translation initiation and retained phosphatase activity toward PI(3,4)P_2. In contrast, the *Inpp4a*$^{\Delta Ex23}$-encoded protein had no enzymatic activity. These data indicate that the N-terminal truncated

Inpp4a with phosphatase activity is responsible for the attenuated cerebellar phenotype in the cerebellum of *Inpp4a*$^{\Delta Ex1,2}$ KO mice (Fig. 8). These differences in phosphatase activities possibly explain the phenotypic diversity in the cerebellum caused by different *Inpp4a* mutations. In addition, *Inpp4a* mutant mice are good models of human diseases caused by *INPP4A* mutations, which also exhibit symptomatic diversity. There are registrations of nonsense mutations within many *INPP4A* exons in the dbSNP database (https://www.ncbi.nlm.nih.gov/snp/), which seem pathogenic (Table S1). It is possible that there are unreported novel human *INPP4A* mutant diseases.

Western blotting indicated two Inpp4a isoforms in the wild-type cerebellum. A comparison of RNA-seq data between wild-type forebrain and cerebellum revealed an alternative exon in the cerebellar transcripts. This cerebellar exon encodes a putative transmembrane domain and is known as INPP4 type I beta (Norris et al., 1997). This isoform had no phosphatase activity when expressed in bacteria or insect SF9 cells (Norris et al., 1997). In this study, transfection in mammalian HEK293 cells revealed that only the wild-type Inpp4a isoform has phosphatase activity toward PIP_2, while the cerebellar Inpp4a (Inpp4a beta) isoform does not. Because homozygous mutation in the cerebellar INPP4A isoform leads to neurological disorder without CNS malformation (Najmabadi et al., 2011), the isoform with the C2 domain and putative transmembrane domain has specific function(s) other than phosphatase activity. One possible function is synaptic modulation (Cremona and de Camilli, 2001; Sasaki et al., 2010) because Synaptotagmin (Chapman, 2002) also has C2 and transmembrane domains. The second possibility is a nuclear function, such as the stress response (Gozani et al., 2003) or DNA repair, similar to INPP4B (Sun et al., 2020). Notably, there is also an INPP4B isoform with a putative transmembrane domain at the C-terminus (Norris et al., 1997).

In the *Inpp4a*$^{\Delta Ex1,2}$ brain, we observed neuronal cell degeneration in the striatum but not in cerebellar Purkinje cells. A possible reason for this is that the high promoter activity of

Inpp4a in Purkinje cells allows *Inpp4a* mRNA to be present in large quantities, allowing sufficient truncated Inpp4a protein to be produced despite less effective alternative translation initiation. Another possibility is that striatal neurons are more sensitive to reduced levels of Inpp4a and phosphatase activity; for example, less Inpp4b in the striatum leads to less redundancy. Alternatively, the function of the N-terminal C2 domain may be essential for the survival of striatal neurons. Alternative translation initiation occurs in many other genes (Gurvich et al., 2009; Lock et al., 1991; Xu and Zhang, 2020), and in the generation of knockout mice, knocking out the exon encoding the first ATG sometimes results in a hypomorphic instead of a null allele that can result in a weak phenotype (Motley et al., 2020; Zhou et al., 2022). Recent studies have reported human genetic diseases associated with variation in the human *INPP4A* gene. These diseases have diverse manifestations with or without cerebellar symptoms (Banihashemi et al., 2020; Hecher et al., 2023; Najmabadi et al., 2011; Özkan Kart et al., 2023; Sheffer et al., 2015). This diversity could be caused by the location of the *INPP4A* mutations. It is possible that the N-terminal-truncated INPP4A protein is produced from an *INPP4A* mutant allele, such as p.(Gln39*) mutation (Banihashemi et al., 2020). Indeed, $Inpp4a^{\Delta Ex1,2}$ transcripts isolated by RT-PCR from $Inpp4a^{\Delta Ex1,2}$ KO mice have a sequence in exon 3 that corresponds to a Kozak sequence (Kozak, 1977). It is also possible that translation initiation can start from a non-ATG codon (Florkiewicz and Sommer, 1989).

The N-terminal truncated Inpp4a protein expressed from the $Inpp4a^{\Delta Ex1,2}$ allele formed aggregate-like structures in the cytoplasm when we examined subcellular localization in transfected cells. Notably, Inpp4a proteins contain multiple ATG8-interacting (WxxL) motifs (Noda et al., 2010), some of the motifs may have a functional interaction with ATG8, an autophagy-related protein required for autophagosome formation. Furthermore, the N-terminal truncated Inpp4a protein lacking the C2 domain may result in abnormal intracellular

localization of the protein and influence the regulation of autophagy, which may explain the aggregation-like structure after its over-expression.

In the present study, we analyzed two strains of *Inpp4a* mutant mice with or without cerebellar degeneration. We found low levels of N-terminal-truncated Inpp4a via alternative translation initiation in *Inpp4a*$^{\Delta Ex1,2}$ KO mice with phosphatase activity for PIP_2. In contrast, the mutant Inpp4a protein expressed from the *Inpp4a*$^{\Delta Ex23}$ allele did not exhibit phosphatase activity for PIP_2. The phosphatase activity may account for the attenuated cerebellar phenotypes in the *Inpp4a*$^{\Delta Ex1,2}$ KO mice. These *Inpp4a* mutant mouse strains are good models for developing new treatment strategies for human INPP4A disease, which has diverse symptoms.

Materials and Methods

Animals. We transferred two *Inpp4a* mutant lines of C57BL/6J background from Tokyo Medical and Dental University to Niigata University: *Inpp4a*^{tm1Tsak} mice (MGI:4462378) (Sasaki et al., 2010) and *Inpp4a*^{flox} mice (Nigorikawa et al., 2015). In this study, *Inpp4a*^{tm1Tsak} allele is also called *Inpp4a*$^{\Delta Ex1,2}$, which lacks part of the N-terminal C2 domain. In the *Inpp4a*^{flox} allele, two loxP sites are located upstream and downstream of exon 23, encoding part of the phosphatase domain (Peters et al., 1998). To generate *Inpp4a*$^{\Delta Ex23}$ allele, we crossed *Inpp4a*^{flox} mice with β-*actin* (*Actb)-iCre-IRES-Green Fluorescent Protein (GFP)* knockin mice of C57BL/6N background (Zhou et al., 2018). Double heterozygous mice (*Actb-iCre-IRES-GFP*;*Inpp4a* $^{flox/+}$) were crossed with C57BL/6N mice to generate the *Inpp4a* KO allele lacking exon 23 (*Inpp4a*$^{\Delta Ex23}$). *Inpp4a* KO mice (*Inpp4a*$^{\Delta Ex1,2/\Delta Ex1,2}$ or *Inpp4a*$^{\Delta Ex23/\Delta Ex23}$) were generated by crossing heterozygous pairs. For conditional knockout (cKO) experiments, we used *En1*$^{tm2(Cre)Wrst}$ (MGI:2446434, Kimmel et al., 2000). We crossed female *Inpp4a*$^{flox/flox}$ mice with male *En1-Cre;Inpp4*$^{flox/+}$ to obtain *En1-Cre;Inpp4a* cKO (*En1-Cre;Inpp4a*$^{flox/flox}$) mice. The

mice were maintained at 22°C ± 2°C and 60% humidity on a 12-hr light/dark cycle. Food and water were freely accessible. Animal care and experimental protocols were approved by the Animal Experiment Committee of Niigata University and Tokyo Medical and Dental University. We used male and female mice at 1–3 weeks old.

Genotyping PCR. Genotyping PCR for the *Inpp4a*$^{\Delta Ex1,2}$ allele was performed as previously described (MGI:4462378, Sasaki et al., 2010). Primers used to detect *Inpp4a*^{flox} and *Inpp4a*$^{+}$ alleles were previously described (Morioka et al., 2022). *Inpp4a*$^{\Delta Ex23}$ allele was detected using the following primers (5'-AGG GTC AGT GTG AAG CAG TGA TG-3' and 5'-TGT CGC CAC TTT TGC TCC TAT C-3'), which produce 510bp-product from *Inpp4a*$^{\Delta Ex23}$ allele and 1350bp-product from wild-type allele. For genotyping of *Actb-iCre-IRES-GFP* knockin mice (Zhou et al., 2018), iCre 538 primers (iCre 538-F 5'-CTC AAC ATG CTG CAC AGG AGA T-3' and iCre 538-R 5'-ACC ATA GAT CAG GCG GTG GGT-3') were used to amplify 538bp-fragments from *iCre* transgene. PCR was performed using Quick Taq HS Dye Mix (Toyobo, Osaka, Japan) and PCR Cyclers (TaKaRa bio, Shiga, Japan) under the following PCR conditions: 95 °C for 30 s, 30 cycles of 95 °C for 10 s, 60 °C for 30 s, and 72 °C for 30 s, followed by 72 °C for 60 s. The PCR products were separated by electrophoresis on 2% agarose gel.

Histology. Paraffin sections for immunohistochemistry (IHC) and *in situ* hybridization (ISH) were prepared as previously described (Takebayashi et al., 2000; Yoshioka et al., 2020). Consecutive 10-μm-thick coronal and sagittal sections of brains were cut using a rotary paraffin microtome (HM 325; Microm, Walldorf, Germany). The following primary antibodies were used: mouse anti-Calbindin-D antibody (1:10,000, Cat#300, Swant), rabbit anti-cleaved Caspase-3 (1:400; Cat#9664, Cell Signaling Technology), rabbit anti-ssDNA antibody (1:100, Cat#18731, IBL), rabbit anti-GFAP (glial fibrillary acidic protein) (1:100, Cat#442251, Nichirei), rat anti-Inpp4a antibody (1:500; homemade, Immunogen is 492-530 aa of mouse

Inpp4a), rabbit anti-Iba1 (1:2,000, Cat#019-19741, WAKO), and rabbit phospho-Akt (1:100, Cat#4060, Cell Signaling Technology). In addition, peroxidase-conjugated secondary antibodies were used, including goat anti-rabbit IgG antibody (1:200, Cat.#458, MBL, Nagoya, Japan), goat anti-mouse IgG antibody (1:200; Cat.#330, MBL), rabbit anti-goat IgG antibody (1:200; Cat.#546, MBL), or rabbit anti-rat IgG antibody (1:200; Cat.#P0450, Dako). After 3,3'-Diaminobenzidine staining, sections were mounted with coverslips. For fluorescent IHC, the following secondary antibodies were used: Alexa Fluor488-conjugated goat anti-rabbit IgG antibody (1:1,000; Cat.#A11034, Invitrogen/Thermo Fisher Scientific), Alexa Fluor594-conjugated goat anti-mouse IgG antibody (1:1,000; Cat.#A11032, Invitrogen/Thermo Fisher Scientific). Quantification of ssDNA, cl-Casp3, Iba1, and GFAP was performed by MetaMorph software (Meta Series Software ver. 7.10.2; Molecular Devices, San Jose, CA, USA). The number of positive signals was normalized by the area of the cerebellum (ssDNA, cl-Casp3) or the striatum (Iba1, GFAP) in each section. Quantification analysis was performed on three sections per mouse, with three or more mice per group.

As previously described, ISH was performed on paraffin sections (Horie et al., 2014; Takebayashi et al., 2000) using a mouse *Inpp4a* probe (GenBank accession number: NM_030266, nt 927–1825). After ISH, sections were counterstained by Nuclear Fast Red. Light microscopic images were taken using a microscope (BX53, Olympus) connected to a CCD camera (DP74; Olympus) or a confocal microscopy FV-1200 (Olympus).

RNA-seq analyses. RNA-seq was performed according to previous reports (Bizen et al., 2022; Yoshioka et al., 2022). RNA was extracted from the wild-type forebrain after removing the olfactory bulb and wild-type cerebellum at postnatal days 14 (P14) using RNeasy Mini Kit (QIAGEN).

Real-time PCR. Total RNA was extracted from the mouse brain using the Rneasy Mini Kit (QIAGEN), including DNase digestion. 100 ng of RNA template was used for cDNA

synthesis with oligo (dT) primers. Real-time PCR was performed using a StepOnePlus Real-Time PCR system (Thermo Fisher Scientific) and the following cycling conditions: 95°C for 2 min, followed by 40 cycles of 95°C for 15 s and 60°C for 40 s, and then, 95°C for 15 s, 60℃ for 1 min, 95℃ for 15 s. Gene expression levels were analyzed using the ΔΔCT method. *Gapdh* was used as an internal control for normalization. The primers used for real-time PCR are as follows: Inpp4a forward: 5′-ACT CCA TCG CTA GAT CGA AAA CC-3′ & Inpp4a reverse: 5′-AGG CAA TGC TGC TTA GAA AGA T-3′ (for *Inpp4a* in Fig. 3), Exon 22 forward: 5′-TCT ACC TCG ATC TCG GAG TCA-3′ & Exon 22 reverse: 5′-TGC GTG CAT GGA CAT TCT GT-3′ (for total *Inpp4a*), Exon 24 forward: 5′-ACC CAG AAG AAC TTG AGC GG-3′ & Exon 24 reverse: 5′-CAC CAG GTA CGC TAT GCT CA-3′ (for *Inpp4a beta*), Exon 25 forward: 5′-GTT GTC GGC GAG AAA ACA CA-3′ & Exon 25 reverse: 5′-CGT AAG TCC CTT CTG GAG GC-3′ (for *Inpp4a alpha*), and *Gapdh* forward 5′-AGG TCG GTG TGA ACG GAT TTG-3′ & *Gapdh* reverse 5′-TGT AGA CCA TGT AGT TGA GGT CA-3′ (for internal control).

Construction of mouse Inpp4a expression plasmids. Mouse *Inpp4a* cDNAs with C-terminal FLAG tag were generated by PCR using mouse cerebellum cDNAs (wild-type, $Inpp4a^{\Delta ex1,2}$ KO, and $Inpp4a^{\Delta ex23}$ KO mice) as templates. The primers were 5′-GGG GTA CCC CCC ACG TGG TCC AAA AGC AAG-3′ (sense), 5′-ATA AGA ATG CGG CCG CAA GCT TTC ACT TGT CAT CGT CAT CCT TGT AGT CTG TCT CAA CTT TTC CGT AAG TCC CT-3′ (antisense for Inpp4a WT, Δ2, Δ23), and 5′-ATA AGA ATG CGG CCG CAA GCT TTC ACT TGT CAT CGT CAT CCT TGT AGT CCG GGC ACT TTT GTC TGC CTC-3′ (antisense for Inpp4a CB). TaKaRa LA Taq (TaKaRa Bio Inc.) was used for the PCR reactions. The PCR products containing the full-length *Inpp4a* cDNAs with FLAG tag were cut with Asp718 (Roche) and NotI (Nippon Gene) and then subcloned into pcDNA3 plasmid vector (Invitrogen). The produced plasmids were referred as pcDNA3-mouse Inpp4a-FLAG, pcDNA3-

mouse Inpp4a ΔEx1,2-FLAG, pcDNA3-mouse Inpp4a ΔEx23, and pcDNA3-mouse Inpp4a CB-FLAG plasmids. Sequencing was performed on both strands.

Cell culture, Transfection, and Immunocytochemistry. Cell culture, transfection, and immunocytochemistry were performed as previously described with minor modifications (Bizen et al., 2022). NIH3T3 cells (Thumkeo et al., 2011) were plated on coverslips pre-coated with poly-L-ornithine (Sigma-Aldrich) and fibronectin (Thermo Fisher Scientific) and cultured in DMEM medium with 10% fetal bovine serum. The next day, pcDNA3-mouse Inpp4a-FLAG, pcDNA3-mouse Inpp4a ΔEx1,2-FLAG, pcDNA3-mouse Inpp4a ΔEx23, and pcDNA3-mouse Inpp4a CB-FLAG plasmids were transfected into NIH3T3 cells using Lipofectamine 3000 (Thermo Fisher Scientific) according to the manufacturer's protocol. Forty-eight hours after transfection, the cells were fixed with 4% PFA for 15 min. After washing three times with PBS, the cells were incubated for 1 hour with PBST (PBS and 0.1% Triton X-100) containing 10% goat serum for blocking and permeabilization. The cells were further incubated with rabbit polyclonal FLAG antibody (1:1000; Cat#M185-3L, MBL) and α-Tubulin antibody (1:1000; Cat#3873, Cell Signaling Technology) in antibody solution (PBST and 10% goat serum) overnight at 4°C. On the following day, the cells were washed three times with PBST and then incubated with an antibody solution containing secondary antibodies for 1 hour at room temperature. After washing three times with PBST, the cells were incubated with 4′,6-diamino-2-phenylindole (DAPI) (Dojindo) for counter staining and washed three times with PBS. The images were collected using an Olympus microscope (BX53, Olympus) and a digital camera system (DP74, Olympus).

Western blotting. Protein lysates from CNS tissues and cultured cells were prepared as previously described (Bizen et al., 2022; Yoshioka et al., 2022). After transfection to HEK293T cells using Polyethylenimine (PEI) Max (Polysciences, purchased from Cosmo Bio) according to the manufacturer's protocol, western blotting was performed as previously

described (Bizen et al., 2022). The following antibodies were used: rat monoclonal anti-Inpp4a antibody (1:2,000; homemade), mouse monoclonal FLAG antibody (1:1,000; Cat#F1804, Sigma), rabbit anti-GFP antibody (1:20,000, MBL), and mouse monoclonal anti-β-Actin antibody (1:20,000; Cat#A5441, Sigma).

Measurement of phosphatase activity of Inpp4a proteins. FLAG-tagged Inpp4a, Inpp4a ΔEx1,2, Inpp4a ΔEx23, or Inpp4a CB was expressed in HEK293T cells and purified using an anti-FLAG antibody (Sigma-Aldrich) as previously described (Kofuji et al., 2015). Recombinant Inpp4a-FLAG, Inpp4a ΔEx1,2-FLAG, Inpp4a ΔEx23-FLAG, or Inpp4a CB-FLAG (50 ng) was incubated for 30 minutes at 37°C with 5 to 10 μmol/L 16:0/16:0 PtdIns(3,4)P_2 (Cayman Chemical), 18:1/18:1 PtdIns(3,4)P_2 (Avanti Polar Lipids), and 18:0/20:4 PtdIns(3,4)P_2 (Avanti Polar Lipids) in 25 mmol/L HEPES (pH7.4) plus 100 mmol/L NaCl and 2 mmol/L DTT. Each enzyme heat-treated at 80°C for 10 min was used as a control. Degradation of PtdIns(3,4)P_2 and production of PdInsP were detected by LC-MS/MS method (Koizumi et al., 2019). Especially the production of PdIns(3)P was determined by the PRMC-MS (Phosphoinositide Regioisomer Measurement by Chiral column chromatography and Mass Spectrometry) method (Morioka et al., 2022). Briefly, the reaction mixture was transferred to a glass tube and mixed with 700 μL of methanol/chloroform (1/1) containing 1 nmol of 8:0/8:0 PI(4,5)P_2 (as an absorption inhibitor, Cayman Chemical) and 10 pmol each of synthetic C17:0/C20:4 phosphoinositides (Avanti Polar Lipids) as internal standards, followed by a methylation reaction using 75 μL of trimethylsilyl diazomethane (Tokyo Chemical Industry) for 5 min at room temperature. After the reaction was quenched with 7.5 μL of glacial acetic acid, the sample was mixed with 700 μL methanol/chloroform (1/1), followed by vortexing for 1min. After centrifugation at 1200×g for 3 min, the lower phase was taken to dry under a stream of nitrogen, then re-dissolved in 100 μL methanol (for the C18 column) or acetonitrile (for the

chiral column). The level of methylated phosphoinositides was measured by LC-MS/MS under the same condition as described (Koizumi et al., 2019; Morioka et al., 2022).

Rotarod test. The rotarod test was performed as previously described (Yoshioka et al., 2022). The latency to fall from a rotating rod (30 mm diameter) with an acceleration from 10 to 150 rpm was measured. Each trial was performed for 3 min. In each mouse, two trials were conducted in a day.

Statistical analysis. Data sets from 2 groups or more were analyzed by Student's *t*-test or ANOVA with appropriate post hoc test, respectively. All data sets were tested for normal distribution. If data were not normally distributed, appropriate nonparametric tests were performed. Statistical analysis was performed using ANOVA4 on the Web (https://www.hju.ac.jp/~kiriki/anova4/). Data are presented as the mean ± SD. A p value less than 0.05 was considered significant. *P* values and statistical tests used are indicated in the figure legends. No statistical methods were used to predetermine sample sizes. The sample size was determined empirically using criteria commonly employed in the field. No data were excluded from analyses.

Study approval. All experimental protocols were conducted following the guidelines for animal care regulated by the animal committee of Niigata University and Tokyo Medical Dental University, Japan.

Acknowledgements

We thank Dr. Alex Joyner for *En1-Cre* mice, Dr. Kenji Sakimura and Dr. Manabu Abe for *Actb-iCre-IRES-GFP* mice, Dr. Tomoyuki Fukuda for discussion, and all members of the Takebayashi lab, especially Dr. Li Zhou and Mr. Shusuke Akachi for their technical assistance. We thank Dr. Jeremy Allen from Edanz for editing a draft of this manuscript.

Author contributions

JS, TS, and HT designed the project. DMT, NY, and HT conducted most of the experiments, acquiring and analyzing data, YM-O and NB performed expression vector construction and immunocytochemistry, respectively. MY contributed RNA-seq analyses, and SY, JH, JS, and TS performed phosphatase assay. In addition, SM, MH, JS, TS, and HT provided reagents, DMT and HT wrote the manuscript, and all authors agreed on the final version.

Funding

This study was supported by Grants-in-aid for Scientific Research from Japan's Ministry of Education, Culture, Sports, Science, and Technology (18H02592, 21H02652). This study was supported by a grant from the Uehara Memorial Foundation (HT), Ono Medical Research Foundation (NY), and Kyowa-kai General Incorporated Foundation (DMT). This study was partly supported by Nanken-Kyoten and Medical Research Center Initiative for High Depth Omics, TMDU. In addition, DMT was supported by the MEXT scholarship.

Data availability

The sequence reported in this paper has been deposited in the Gene Expression Omnibus (GEO) database, www.ncbi.nlm.nih.gov/geo (accession number GSE221867). All other relevant data can be found within the article and its supplementary information.

Competing interests

The authors declare no competing or financial interests.

References

Aich, J., Mabalirajan, U., Ahmad, T., Agrawal, A. and Ghosh, B. (2012). Loss-of-function of inositol polyphosphate-4-phosphatase reversibly increases the severity of allergic airway inflammation. *Nat Commun* **3**, 877.

Balla, T. (2013). Phosphoinositides: Tiny Lipids With Giant Impact on Cell Regulation. *Physiol Rev* **93**, 1019–1137.

Banihashemi, S., Tahmasebi-Birgani, M., Mohammadiasl, J. and Hajjari, M. (2020). Whole exome sequencing identified a novel nonsense INPP4A mutation in a family with intellectual disability. *Eur J Med Genet* **63**, 103846.

Bizen, N., Bepari, A. K., Zhou, L., Abe, M., Sakimura, K., Ono, K. and Takebayashi, H. (2022). Ddx20, an Olig2 binding factor, governs the survival of neural and oligodendrocyte progenitor cells via proper Mdm2 splicing and p53 suppression. *Cell Death Differ* **29**, 1028–1041.

Bunney, T. D. and Katan, M. (2010). Phosphoinositide signalling in cancer: beyond PI3K and PTEN. *Nat Rev Cancer* **10**, 342–352.

Chapman, E. R. (2002). Synaptotagmin: A Ca2+ sensor that triggers exocytosis? *Nat Rev Mol Cell Biol* **3**, 498–508.

Cremona, O. and de Camilli, P. (2001). Phosphoinositides in membrane traffic at the synapse. *J Cell Sci* **114**, 1041–1052.

Echard, A. (2012). Phosphoinositides and cytokinesis: The “PIP” of the iceberg. *Cytoskeleton* **69**, 893–912.

Florkiewicz, R. Z. and Sommer, A. (1989). Human basic fibroblast growth factor gene encodes four polypeptides: three initiate translation from non-AUG codons. *Proc Natl Acad Sci USA,* **86**, 3978–3981.

Fukumoto, M., Ijuin, T. and Takenawa, T. (2017). PI(3,4)P $_2$ plays critical roles in the regulation of focal adhesion dynamics of MDA-MB-231 breast cancer cells. *Cancer Sci* **108**, 941–951.

Gozani, O., Karuman, P., Jones, D. R., Ivanov, D., Cha, J., Lugovskoy, A. A., Baird, C. L., Zhu, H., Field, S. J., Lessnick, S. L., et al. (2003). The PHD Finger of the Chromatin-Associated Protein ING2 Functions as a Nuclear Phosphoinositide Receptor. *Cell* **114**, 99–111.

Gurvich, O. L., Maiti, B., Weiss, R. B., Aggarwal, G., Howard, M. T. and Flanigan, K. M. (2009). *DMD* exon 1 truncating point mutations: Amelioration of phenotype by alternative translation initiation in exon 6. *Hum Mutat* **30**, 633–640.

Hawkins, P. T. and Stephens, L. R. (2016). Emerging evidence of signalling roles for PI(3,4) *P* 2 in Class I and II PI3K-regulated pathways. *Biochem Soc Trans* **44**, 307–314.

Hecher, L., Harms, F. L., Lisfeld, J., Alawi, M., Denecke, J. and Kutsche, K. (2023). INPP4A-related genetic and phenotypic spectrum and functional relevance of subcellular targeting of INPP4A isoforms. *Neurogenetics* **24,** 79–93.

Horie, M., Watanabe, K., Bepari, A. K., Nashimoto, J., Araki, K., Sano, H., Chiken, S., Nambu, A., Ono, K., Ikenaka, K., et al. (2014). Disruption of actin-binding domain-containing Dystonin protein causes *dystonia musculorum* in mice. *Eur J Neurosci* **40**, 3458–3471.

Kim, J.-S., Yun, H. S., Um, H.-D., Park, J. K., Lee, K.-H., Kang, C.-M., Lee, S.-J. and Hwang, S.-G. (2012). Identification of inositol polyphosphate 4-phosphatase type II as a novel tumor resistance biomarker in human laryngeal cancer HEp-2 cells. *Cancer Biol Ther* **13**, 1307–1318.

Kimmel, R. A., Turnbull, D. H., Blanquet, V., Wurst, W., Loomis, C. A. and Joyner, A. L. (2000). Two lineage boundaries coordinate vertebrate apical ectodermal ridge formation. *Genes Dev* **14**, 1377–1389.

Kofuji, S., Kimura, H., Nakanishi, H., Nanjo, H., Takasuga, S., Liu, H., Eguchi, S., Nakamura, R., Itoh, R., Ueno, N., et al. (2015). INPP4B Is a PtdIns(3,4,5)P3 Phosphatase That Can Act as a Tumor Suppressor. *Cancer Discov* **5**, 730–739.

Koizumi, A., Narita, S., Nakanishi, H., Ishikawa, M., Eguchi, S., Kimura, H., Takasuga, S., Huang, M., Inoue, T., Sasaki, J., et al. (2019). Increased fatty acyl saturation of phosphatidylinositol phosphates in prostate cancer progression. *Sci Rep* **9**, 13257.

Kozak, M. (1977). Nucleotide sequences of 5′-terminal ribosome-protected initiation regions from two reovirus messages. *Nature* **269**, 390–394.

Lock, P., Ralph, S., Stanley, E., Boulet, I., Ramsay, R. and Dunn, A. R. (1991). Two isoforms of murine hck, generated by utilization of alternative translational initiation codons, exhibit different patterns of subcellular localization. *Mol Cell Biol* **11**, 4363–4370.

Morioka, S., Nakanishi, H., Yamamoto, T., Hasegawa, J., Tokuda, E., Hikita, T., Sakihara, T., Kugii, Y., Oneyama, C., Yamazaki, M., et al. (2022). A mass spectrometric method for in-depth profiling of phosphoinositide regioisomers and their disease-associated regulation. *Nat Commun* **13**, 83.

Motley, W. W., Züchner, S. and Scherer, S. S. (2020). Isoform-specific loss of dystonin causes hereditary motor and sensory neuropathy. *Neurol Genet* **6**, e496.

Najmabadi, H., Hu, H., Garshasbi, M., Zemojtel, T., Abedini, S. S., Chen, W., Hosseini, M., Behjati, F., Haas, S., Jamali, P., et al. (2011). Deep sequencing reveals 50 novel genes for recessive cognitive disorders. *Nature* **478**, 57–63.

Nigorikawa, K., Hazeki, K., Sasaki, J., Omori, Y., Miyake, M., Morioka, S., Guo, Y., Sasaki, T. and Hazeki, O. (2015). Inositol Polyphosphate-4-Phosphatase Type I

Negatively Regulates Phagocytosis via Dephosphorylation of Phagosomal PtdIns(3,4)P2. *PLoS One* **10**, e0142091.

Nilius, B., Owsianik, G. and Voets, T. (2008). Transient receptor potential channels meet phosphoinositides. *EMBO J* **27**, 2809–2816.

Noda, N. N., Ohsumi, Y. and Inagaki, F. (2010). Atg8-family interacting motif crucial for selective autophagy. *FEBS Lett* **584**, 1379–1385.

Norris, F. A., Auethavekiat, V. and Majerus, P. W. (1995). The Isolation and Characterization of cDNA Encoding Human and Rat Brain Inositol Polyphosphate 4-Phosphatase. *J Biol Chem* **270**, 16128–16133.

Norris, F. A., Atkins, R. C. and Majerus, P. W. (1997). The cDNA Cloning and Characterization of Inositol Polyphosphate 4-Phosphatase Type II. *J Biol Chem* **272**, 23859–23864.

Nystuen, A., Legare, M. E., Shultz, L. D. and Frankel, W. N. (2001). A Null Mutation in Inositol Polyphosphate 4-Phosphatase Type I Causes Selective Neuronal Loss in Weeble Mutant Mice. *Neuron* **32**, 203–212.

Özkan Kart, P., Citli, S., Yildiz, N. and Cansu, A. (2023). A novel INPP4A mutation with pontocerebellar hypoplasia, myoclonic epilepsy, microcephaly, and severe developmental delay. *Brain Dev* **45,** 300–305.

Peters, G. H., Frimurer, T. M. and Olsen, O. H. (1998). Electrostatic evaluation of the signature motif (H/V)CX5R(S/T) in protein-tyrosine phosphatases. *Biochemistry* **37**,.

Rahdar, M., Inoue, T., Meyer, T., Zhang, J., Vazquez, F. and Devreotes, P. N. (2009). A phosphorylation-dependent intramolecular interaction regulates the membrane association and activity of the tumor suppressor PTEN. *Proc Natl Acad Sci USA* **106**, 480–485.

Roth, M. G. (2004). Phosphoinositides in Constitutive Membrane Traffic. *Physiol Rev* **84**, 699–730.

Sasaki, T., Takasuga, S., Sasaki, J., Kofuji, S., Eguchi, S., Yamazaki, M. and Suzuki, A. (2009). Mammalian phosphoinositide kinases and phosphatases. *Prog Lipid Res* **48**, 307–343.

Sasaki, J., Kofuji, S., Itoh, R., Momiyama, T., Takayama, K., Murakami, H., Chida, S., Tsuya, Y., Takasuga, S., Eguchi, S., et al. (2010). The PtdIns(3,4)P2 phosphatase INPP4A is a suppressor of excitotoxic neuronal death. *Nature* **465**, 497–501.

Shearn, C. T., Walker, J. and Norris, F. A. (2001). Identification of a Novel Spliceoform of Inositol Polyphosphate 4-Phosphatase Type Iα Expressed in Human Platelets: Structure of Human Inositol Polyphosphate 4-Phosphatase Type I Gene. *Biochem Biophys Res Commun* **286**, 119–125.

Sheffer, R., Bennett-Back, O., Yaacov, B., Edvardson, S., Gomori, M., Werner, M., Fahham, D., Anteby, I., Frumkin, A., Meiner, V., et al. (2015). Hindbrain malformation and myoclonic seizures associated with a deleterious mutation in the INPP4A gene. *Neurogenetics* **16**, 23–26.

Sun, Y., Ning, X., Fan, J., Hu, J., Jiang, Y., Hu, Z., Paulo, J. A., Liu, J., Qiu, X., Xu, H., et al. (2020). Loss of tumor suppressor inositol polyphosphate 4-phosphatase type B impairs DNA double-strand break repair by destabilization of DNA tethering protein Rad50. *Cell Death Dis* **11**, 292.

Thumkeo, D., Shinohara, R., Watanabe, K., Takebayashi, H., Toyoda, Y., Tohyama, K., Ishizaki, T., Furuyashiki, T. and Narumiya S. (2011). Deficiency of mDia, an actin nucleator, disrupts integrity of neuroepithelium and causes periventricular dysplasia. *PLoS One* **6,** e25465.

Takebayashi, H., Yoshida, S., Sugimori, M., Kosako, H., Kominami, R., Nakafuku, M. and Nabeshima, Y. (2000). Dynamic expression of basic helix-loop-helix Olig family

members: implication of Olig2 in neuron and oligodendrocyte differentiation and identification of a new member, Olig3. *Mech Dev* **99**, 143–148.

Vanhaesebroeck, B., Guillermet-Guibert, J., Graupera, M. and Bilanges, B. (2010). The emerging mechanisms of isoform-specific PI3K signalling. *Nat Rev Mol Cell Biol* **11**, 329–341.

Volpatti, J. R., Al-Maawali, A., Smith, L., Al-Hashim, A., Brill, J. A. and Dowling, J. J. (2019). The expanding spectrum of neurological disorders of phosphoinositide metabolism. *Dis Model Mech* **12**, dmm038174.

Waugh, M. G. (2015). PIPs in neurological diseases. *Biochim Biophys Acta* **1851,** 1066–1082.

Wu, Z., Yang, H. and Colosi, P. (2010). Effect of Genome Size on AAV Vector Packaging. Mol Ther **18**, 80–86.

Wu, T., Yin, F., Guang, S., He, F., Yang, L. and Peng, J. (2020). The Glycosylphosphatidylinositol biosynthesis pathway in human diseases. *Orphanet J Rare Dis* **15**, 129.

Xu, C. and Zhang, J. (2020). Mammalian Alternative Translation Initiation Is Mostly Nonadaptive. *Mol Biol Evol* **37**, 2015–2028.

Yang, J., Wu, Z., Renier, N., Simon, D. J., Uryu, K., Park, D. S., Greer, P. A., Tournier, C., Davis, R. J. and Tessier-Lavigne, M. (2015). Pathological Axonal Death through a MAPK Cascade that Triggers a Local Energy Deficit. *Cell* **160**, 161–176.

Yoshioka, N., Kabata, Y., Kuriyama, M., Bizen, N., Zhou, L., Tran, D. M., Yano, M., Yoshiki, A., Ushiki, T., Sproule, T. J., et al. (2020). Diverse dystonin gene mutations cause distinct patterns of *Dst* isoform deficiency and phenotypic heterogeneity in *D ystonia musculorum* mice. *Dis Model Mech* **13**, dmm041608.

Yoshioka, N., Kurose, M., Yano, M., Tran, D. M., Okuda, S., Mori-Ochiai, Y., Horie, M., Nagai, T., Nishino, I., Shibata, S., et al. (2022). Isoform-specific mutation in Dystonin-b gene causes late-onset protein aggregate myopathy and cardiomyopathy. *Elife* **11**, e78419.

Zhang, S.-X., Duan, L.-H., He, S.-J., Zhuang, G.-F. and Yu, X. (2017). Phosphatidylinositol 3,4-bisphosphate regulates neurite initiation and dendrite morphogenesis via actin aggregation. *Cell Res* **27**, 253–273.

Zhou, L., Hossain, M. I., Yamazaki, M., Abe, M., Natsume, R., Konno, K., Kageyama, S., Komatsu, M., Watanabe, M., Sakimura, K., et al. (2018). Deletion of exons encoding carboxypeptidase domain of Nna1 results in Purkinje cell degeneration (*pcd*) phenotype. *J Neurochem* **147**, 557–572.

Zhou, L., Konno, K., Yamazaki, M., Abe, M., Natsume, R., Watanabe, M., Takebayashi, H. and Sakimura, K. (2022). Nna1, Essential for Purkinje Cell Survival, Is also Associated with Emotion and Memory. *Int J Mol Sci* **23**, 12961.

Zolles, G., Klöcker, N., Wenzel, D., Weisser-Thomas, J., Fleischmann, B. K., Roeper, J. and Fakler, B. (2006). Pacemaking by HCN Channels Requires Interaction with Phosphoinositides. *Neuron* **52**, 1027–1036.

Figure legends

Figure 1. Histological analysis of the cerebellum in *Inpp4a*$^{\Delta Ex1,2}$ and *Inpp4a*$^{\Delta Ex23}$ mutant mice.

(A–C) Parasagittal Nissl-stained cerebellum sections of control (Ctrl), *Inpp4a*$^{\Delta Ex1,2}$, and *Inpp4a*$^{\Delta Ex23}$ KO mice at 3 weeks old (n=3 mice, each genotype). (D–F) Calbindin IHC on the parasagittal cerebellum sections of Ctrl, *Inpp4a*$^{\Delta Ex1,2}$, and *Inpp4a*$^{\Delta Ex23}$ KO mice at 3 weeks old (n=3 mice, each genotype). (G–I) Iba1 IHC on the parasagittal cerebellum sections of Ctrl, *Inpp4a*$^{\Delta Ex1,2}$, and *Inpp4a*$^{\Delta Ex23}$ KO mice at 3 weeks old (n=3 mice, each genotype). Insets in Calbindin and Iba1 staining shows the shape of Purkinje cells and microglia, respectively. Scale bars, 200 μm; 50 μm (inset).

Figure 2. Increased apoptotic cells in the *Inpp4a*$^{\Delta Ex23}$ KO cerebellum.

(A–C) Cleaved Caspase-3 (cl-Casp3) IHC on the parasagittal cerebellum sections of control (Ctrl), *Inpp4a*$^{\Delta Ex1,2}$, and *Inpp4a*$^{\Delta Ex23}$ KO mice at 1 week old (n=3 mice, each genotype). Arrowheads indicate cl-Casp3-positive cells. Asterisk indicates cl-Casp3-positive signals in Purkinje cells layer (D–F) Single strand DNA (ssDNA) IHC on the parasagittal cerebellum sections of Ctrl, *Inpp4a*$^{\Delta Ex1,2}$, and *Inpp4a*$^{\Delta Ex23}$ KO mice at 1 week old (n=3 mice, each genotype). Arrowheads indicate ssDNA-positive cells. (G) Quantification of cl-Casp3-positive cells per 1 (mm^2) (A–C). (H) Quantification of ssDNA-positive cells in (D–F). All values in the graphs are presented as means ± SD. Statistical significance was set at a value of $*p<0.05$, $***p<0.001$, $****p<0{,}0001$ (1-way ANOVA). Sample calculation and tests for outliers were not performed. Scale bars, 100 μm (A–F).

Figure 3. Expression of *Inpp4a* mRNA and Inpp4a proteins.

(A–C) *Inpp4a* ISH on parasagittal cerebellum sections of control (Ctrl), *Inpp4a*$^{\Delta Ex1,2}$, and *Inpp4a*$^{\Delta Ex23}$ KO mice at 3 weeks old (n=3 mice, each genotype). Scale bars, 200 μm. (D) quantitative PCR (qPCR) data of *Inpp4a* mRNA in the cerebellum of Ctrl and *Inpp4a*$^{\Delta Ex1,2}$ KO mice at 2 weeks old (n=4 mice, each genotype). All values in the graphs are presented as means ± SD. Statistical significance was set at a value of *p<0.05 (unpaired two-tailed Student's *t*-test). (E) qPCR of *Inpp4a* mRNA in the cerebellum of Ctrl and *Inpp4a*$^{\Delta Ex23}$ KO mice at 3 weeks old (n=3 mice, each genotype). All values in the graphs are presented as means ± SD. Statistical significance was set at a value of *p<0.05, ***p<0.001, ****p<0,0001 (unpaired two-tailed Student's *t*-test). (F) Western blotting by rat monoclonal anti-Inpp4a antibody in the forebrain (FB), hippocampus (Hip), cerebellum (CB), brainstem (BS), and spinal cord (SC) of 3 weeks old of wild-type (WT). There were two Inpp4a bands only in the cerebellum. β-Actin is internal control (n=3 mice). (G) Western blotting by rat monoclonal anti-Inpp4a antibody in the forebrain and cerebellum of WT, *Inpp4a*$^{\Delta Ex1,2}$, and *Inpp4a*$^{\Delta Ex23}$ KO mice at 3 weeks old (n=3 mice, each genotype). Inpp4a bands were significantly diminished in both *Inpp4a*$^{\Delta Ex1,2}$ and *Inpp4a*$^{\Delta Ex23}$ KO mice. β-Actin was used as an internal control.

Figure 4. Identification of cerebellar-specific *Inpp4a* transcripts.

(A) Pile-up view of reads from forebrain and cerebellar RNA-seq data. The black and green arrowheads indicate Exon 16 and Exon 24, respectively. (B–D) qPCR data of *Inpp4a beta* (B), *Inpp4a alpha* (C), and total *Inpp4a* mRNA (D) in the forebrain (FB) and cerebellum (CB) of wild-type (WT) mice at 2 weeks old (n=3 mice, each brain region). For detection of the transcripts, primers corresponding to Exon 25 for *Inpp4a* alpha, Exon 24 for *Inpp4a* beta, or Exon 22 for total *Inpp4a* were used. All values in the graphs are presented as means ± SD. Statistical significance was set at a value of *p<0.05, **p<0.01, ***p<0,001 (unpaired two-tailed Student's *t*-test). “ns” means not significant. (E) Mouse *Inpp4a* genomic structure and

Inpp4a transcripts. The green arrowhead indicates cerebellar-specific exon. Red lines indicate positions of distinct splicing. (F) Alignment of amino acid sequences of mouse Inpp4a isoforms (NCBI accessions: NP_084542.2, XP_006496080.1). UniProt provides the 3D structure of Inpp4a protein (E9Q9A0). The blue box, red, and dark green box indicate the C2 domain, phosphatase domain, and putative transmembrane (TM) domain, respectively. The light green area indicates C-terminus encoded by cerebellar-specific exon. $C(X)_5R$ is an amino acid sequence essential for phosphatase activity. Arrowhead indicates the mutation site of *weeble* mutant mice. The resulting frameshift creates a stop codon at amino acid (aa) position 263. Y indicates the antibody recognition site of rat monoclonal anti-Inpp4a antibody. Note that part of the phosphatase domain is lacking in the cerebellar isoform of the Inpp4a protein.

Figure 5. Expression of Inpp4a isoforms and measurement of phosphatase activity.

(A) Expression of Inpp4a isoforms in HEK293T cells. Inpp4a proteins were detected by western blotting using FLAG antibody (n=3 transfections). Lanes: pcDNA3 & pcDNA3-GFP, pcDNA3-Inpp4a-FLAG & pcDNA3-GFP, pcDNA3-Inpp4a ΔEx1,2-FLAG & pcDNA3-GFP, pcDNA3-Inpp4a ΔEx23-FLAG & pcDNA3-GFP, pcDNA3-Inpp4a CB-FLAG & pcDNA3-GFP. β-Actin was used as an internal control. GFP was used as a control for overexpression. (B) Detection of purified FLAG-tagged Inpp4a proteins by FLAG antibody. Lanes: pcDNA3-Inpp4a-FLAG, pcDNA3-Inpp4a ΔEx1,2-FLAG, pcDNA3-Inpp4a ΔEx23-FLAG, pcDNA3-Inpp4a CB-FLAG, marker. (C) Measurement of phosphatase activity for $PI(3,4)P_2$ of the four FLAG-tagged Inpp4a proteins. Inpp4a-FLAG and Inpp4a ΔEx1,2-FLAG proteins had phosphatase activity, while Inpp4a ΔEx23-FLAG protein and Inpp4a CB-FLAG did not. PI3P production was observed in both Inpp4a-FLAG and Inpp4a ΔEx1,2-FLAG proteins. C32:0, 16:0/16:0 $PtdIns(3,4)P_2$ C36:2, 18:1/18:1 $PtdIns(3,4)P_2$, C38:4, 18:0/20:4 $PtdIns(3,4)P_2$. (D) Immunocytochemistry (ICC) of Inpp4a-FLAG, Inpp4a ΔEx1,2-FLAG, Inpp4a ΔEx23-FLAG, and Inpp4a CB-FLAG protein

after transfection to NIH3T3 cell line (n=2 transfections). Double staining between FLAG-tagged protein (green, upper) and α-Tubulin (red, middle) with DAPI counterstaining (merged, lower). Inpp4a ΔEx1,2-FLAG proteins exhibited aggregate-like structures in the cytoplasm (arrowheads). All values in the graphs are presented as means ± SD. Statistical significance was set at a value of *p<0.05, ***p<0.001 (1-way ANOVA). "ns" means not significant. Scale bar: 20 μm.

Figure 6. Activated Akt signaling in the axons of degenerating Purkinje cells.

(A–C) Double IHC between phospho-Akt (pAkt, Ser 473) and Calbindin on the parasagittal sections of Ctrl (A), *Inpp4a*$^{\Delta Ex1,2}$ (B), and *Inpp4a*$^{\Delta Ex23}$ KO mice (C) at 3 weeks old (n=3 mice, each genotype). Strong pAkt dot signals were observed in the axons of Purkinje cells (arrows) in the cerebellar medulla of *Inpp4a*$^{\Delta Ex23}$ KO mice. There are also pAkt-positive cells (green) in the degenerating *Inpp4a*$^{\Delta Ex23}$ KO cerebellum. Scale bar: 100 μm.

Figure 7. Cerebellar degeneration in the *En1-Cre*;*Inpp4a* cKO mice.

(A) Rotarod test showed less motor coordination of the *En1-Cre;Inpp4a* cKO mice at 3 weeks old (control, n=6 animals; *Inpp4a* cKO, n=5 animals). *p< 0.05, ****p< 0.0001 (unpaired two-tailed Student's *t*-test). (**b, c**) Nissl staining on the parasagittal brain sections of control (Ctrl) (B) and *En1-Cre;Inpp4a* cKO mice (C) at 3 weeks old (n=3 mice, each genotype). *En1-Cre;Inpp4a* cKO mice exhibited cerebellar atrophy. Rectangles indicate cerebellum and striatum area indicated in (D–G) and (H, I), respectively. (D, E) Calbindin IHC on the parasagittal sections of Ctrl (D) and *En1-Cre;Inpp4a* cKO cerebellum (E) at 3 weeks old (n=3 mice, each genotype). Insets show the shape of degenerating Purkinje cells. *En1-Cre;Inpp4a* cKO mice showed cerebellar degeneration. (F, G) Iba1 IHC on the parasagittal sections of Ctrl (F) and *En1-Cre;Inpp4a* cKO striatum (G) at 3 weeks old (n=3 mice, each genotype). Insets

show the shape of microglia. (H, I) Iba1 IHC on the parasagittal sections of Ctrl (H) and *En1-Cre;Inpp4a* cKO striatum (I) at 3 weeks old. Scale bar: 1 mm (B, C), 200 μm (D–G), 100 μm (H–I) and 50 μm (insets of D, E, F, G).

Figure 8. Schematic diagrams of Purkinje cell phenotype.

Schematic diagram of PC phenotype in the wild-type, *Inpp4a*$^{\Delta Ex1,2}$ KO, and *Inpp4a*$^{\Delta Ex23}$ KO mice. We performed Nissl staining on three weeks-old sections. Scale bar: 200 μm.

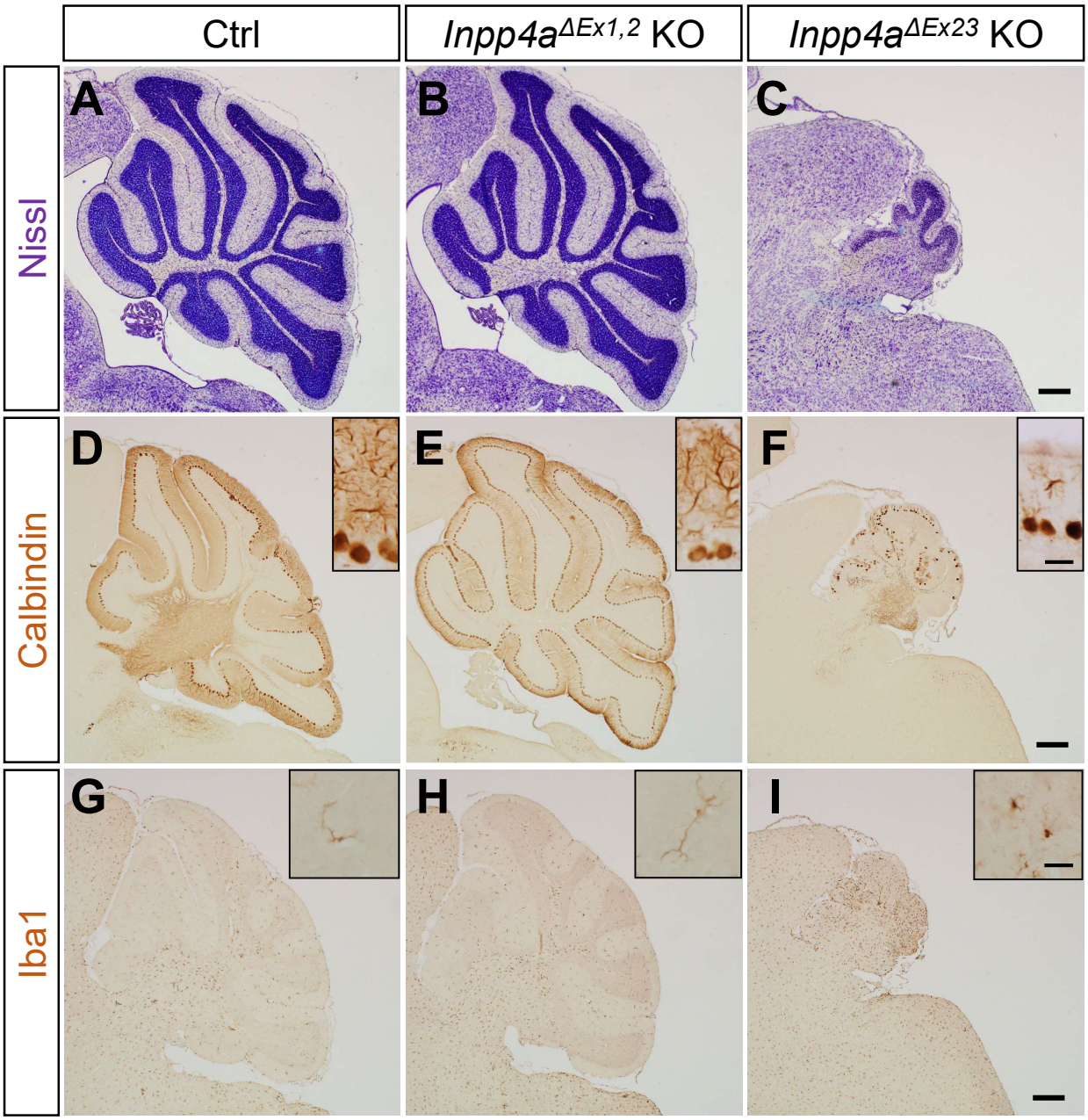

Tran et al., Figure 1

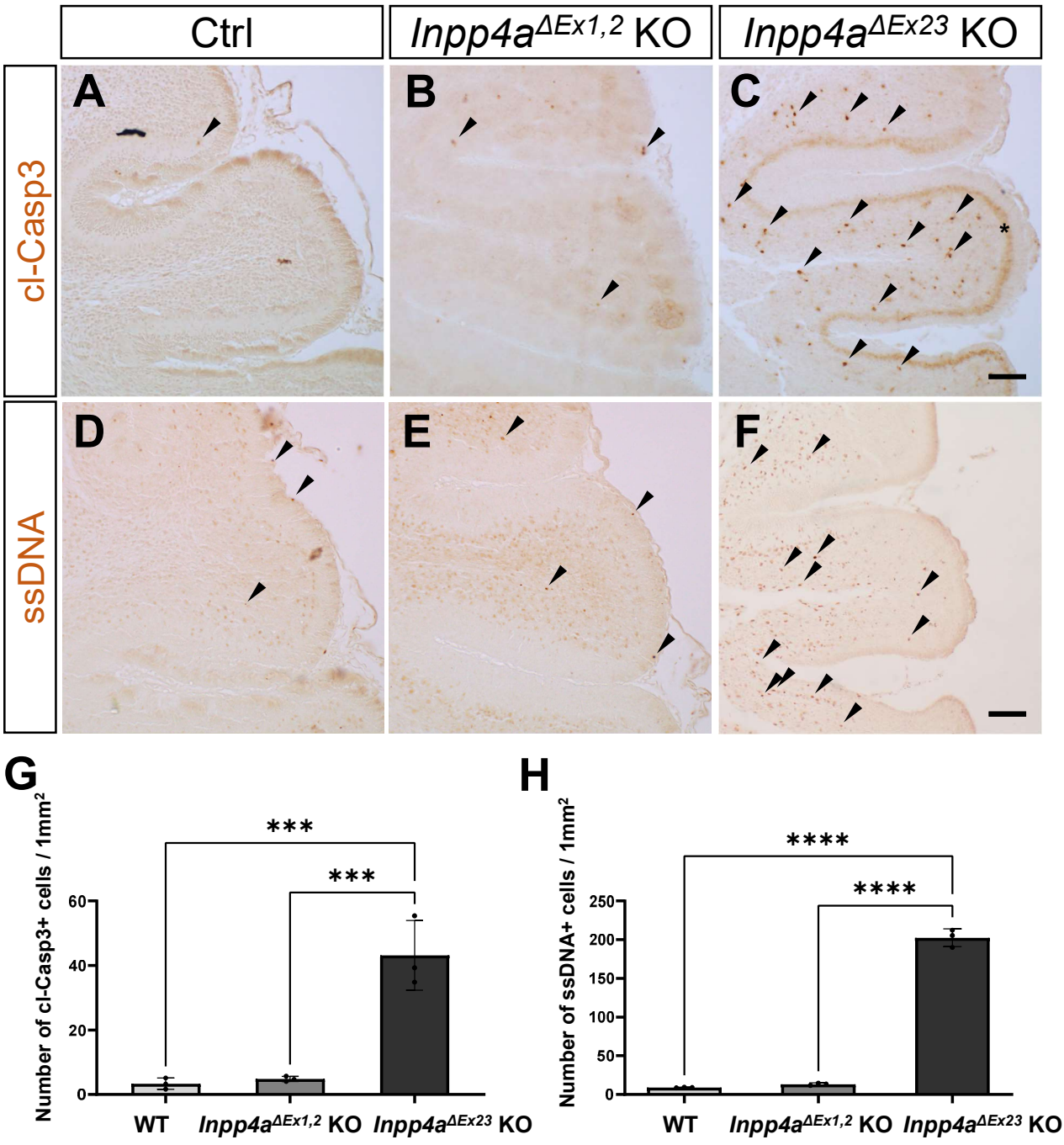

Tran et al., Figure 2

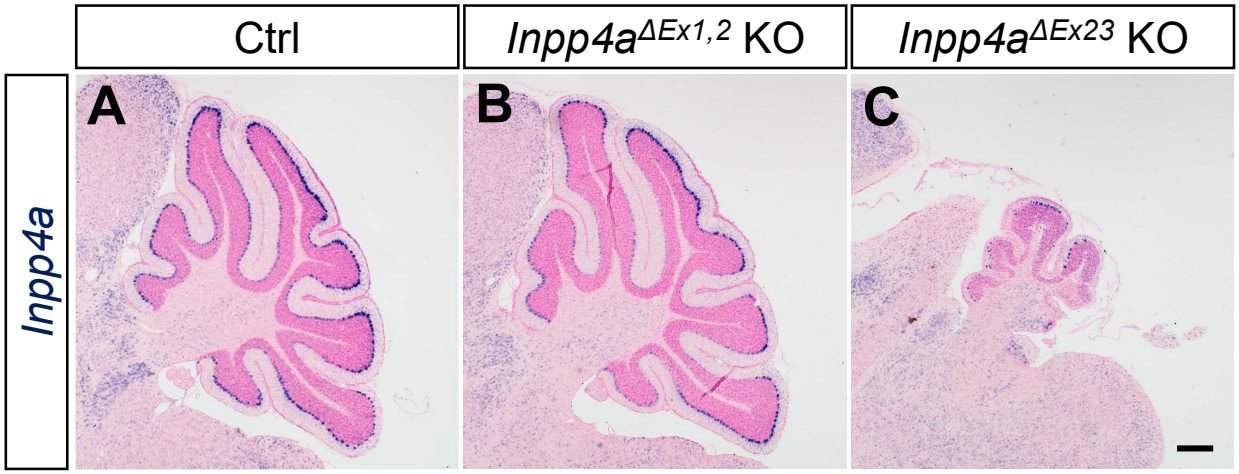

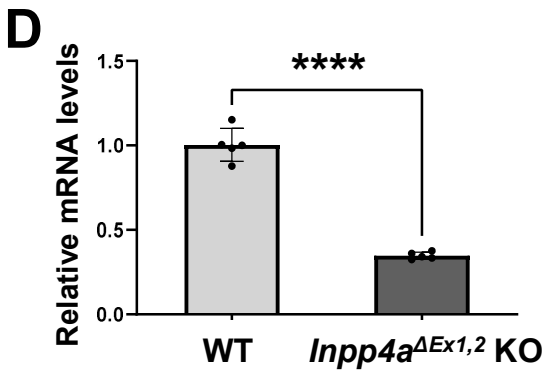

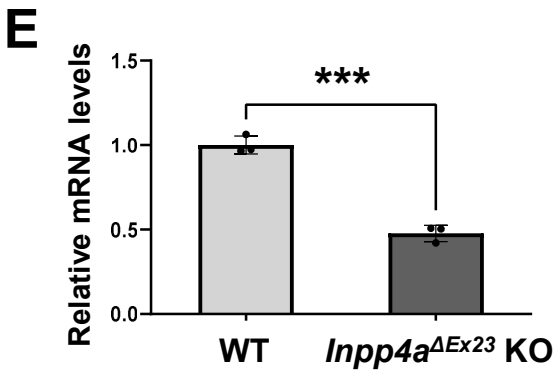

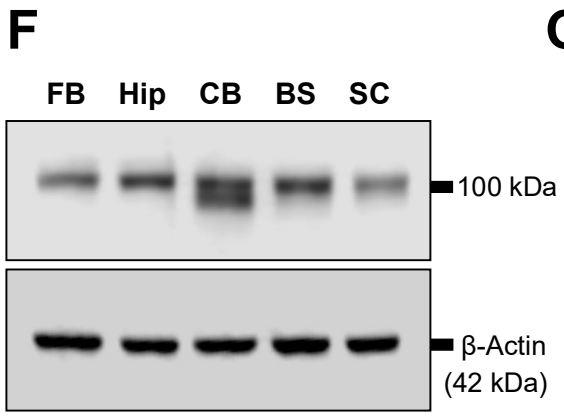

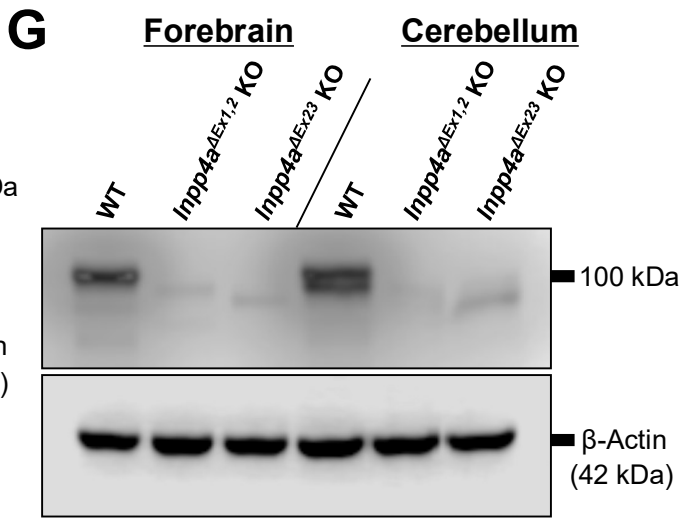

Tran et al., Figure 3

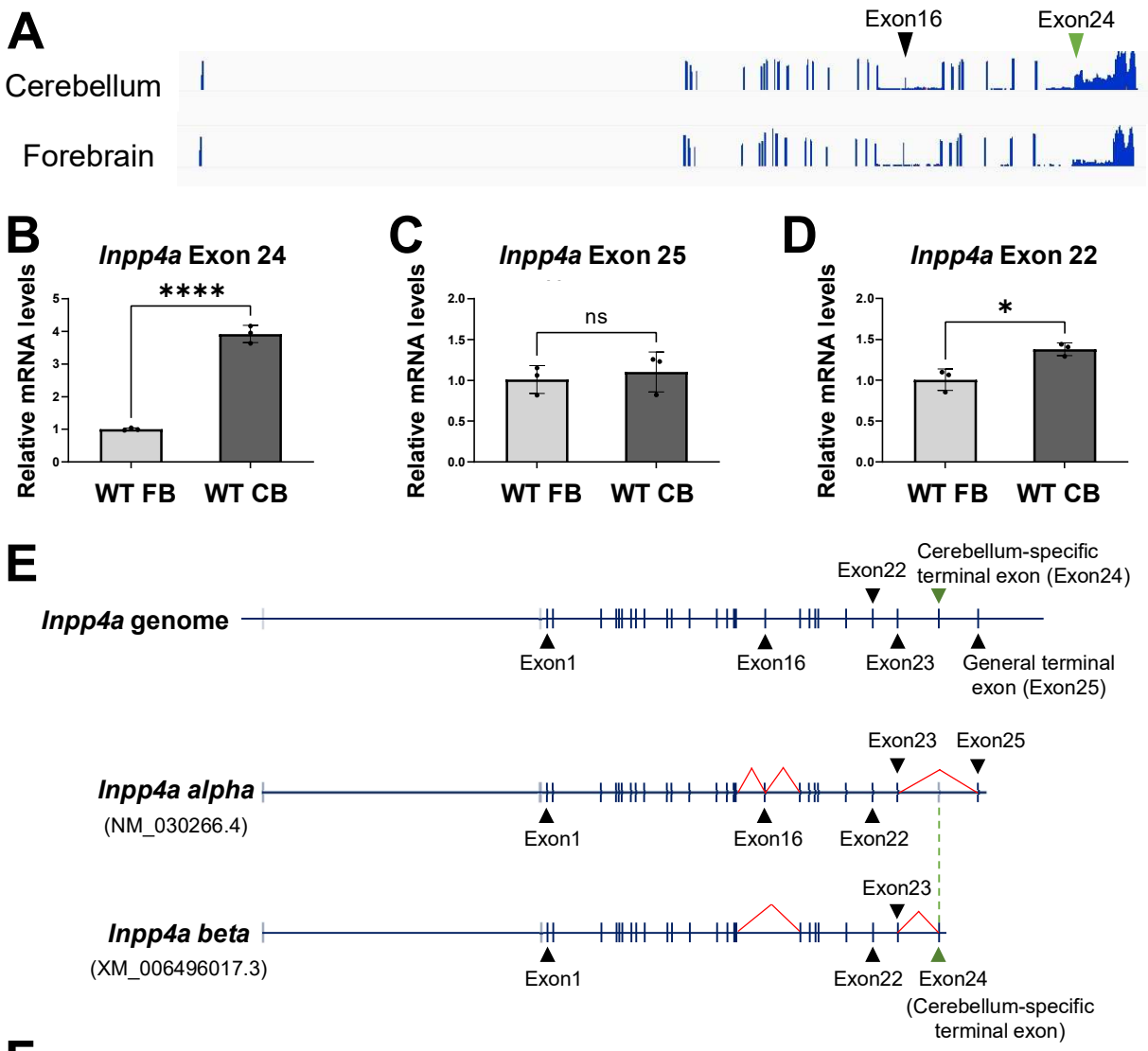

Tran et al., Figure 4

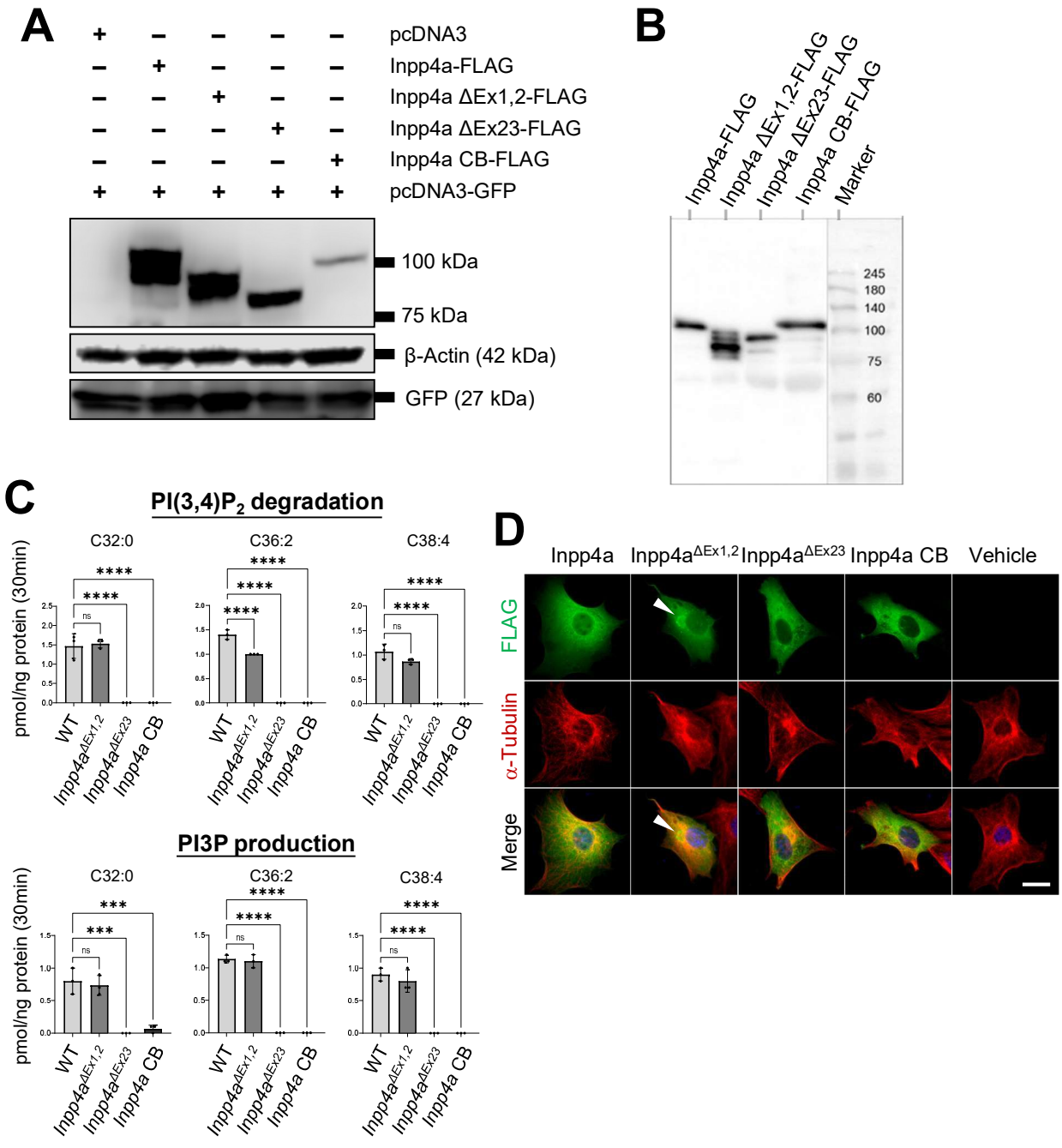

Tran et al., Figure 5

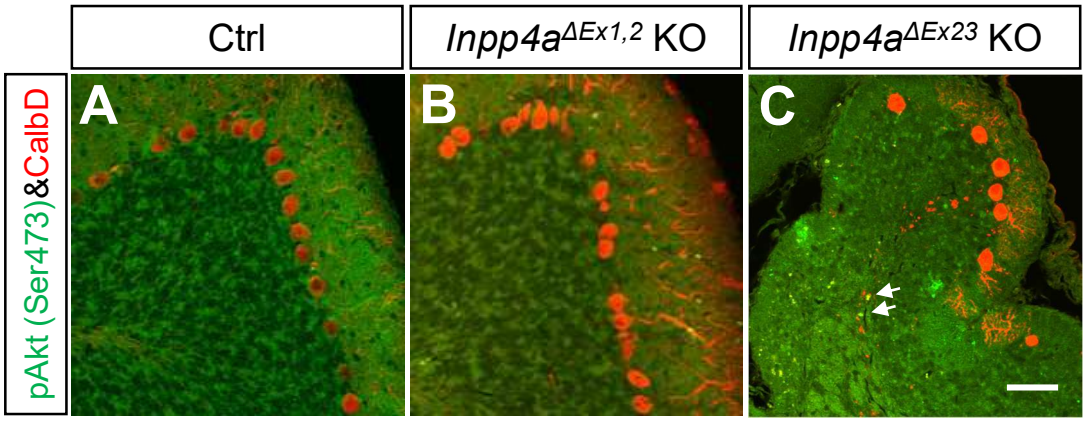

Tran et al., Figure 6

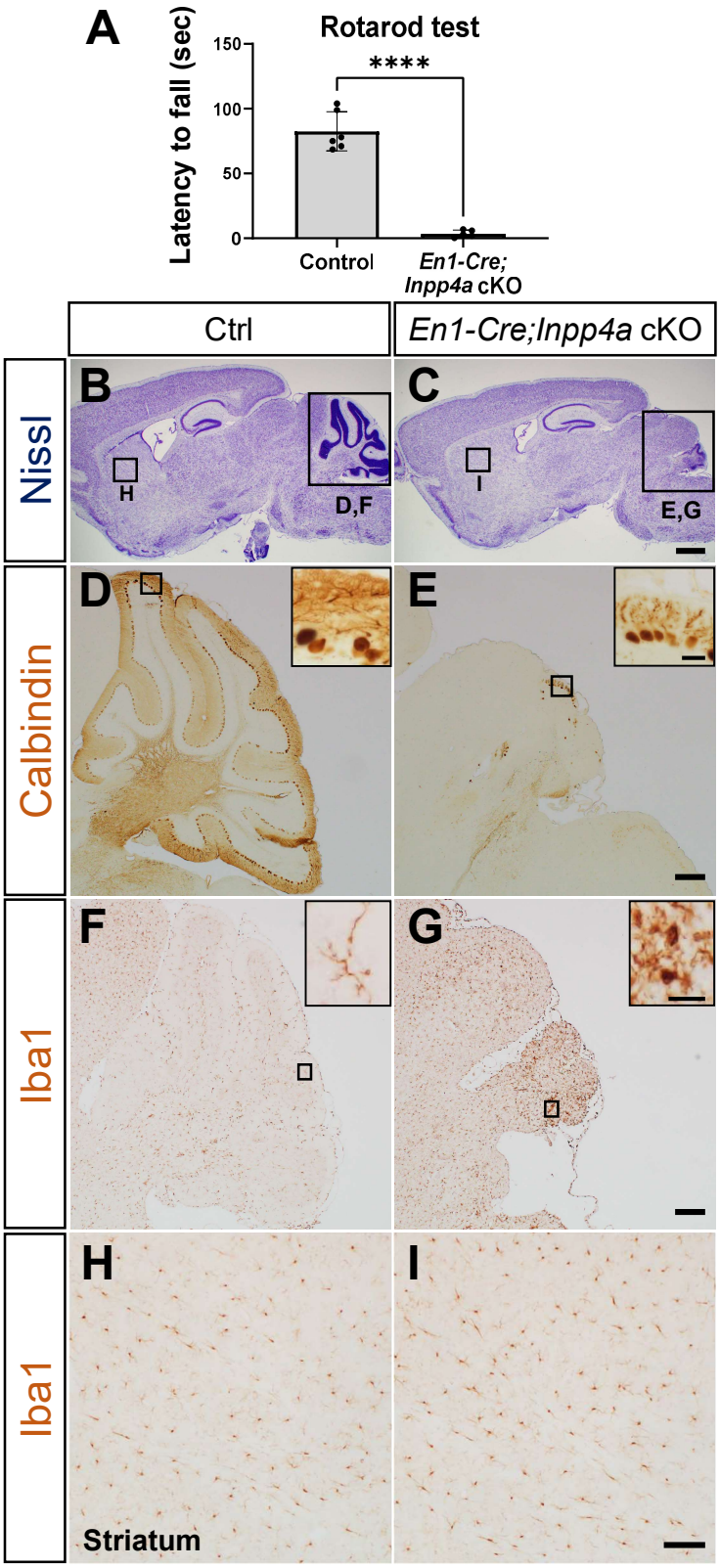

Tran et al., Figure 7

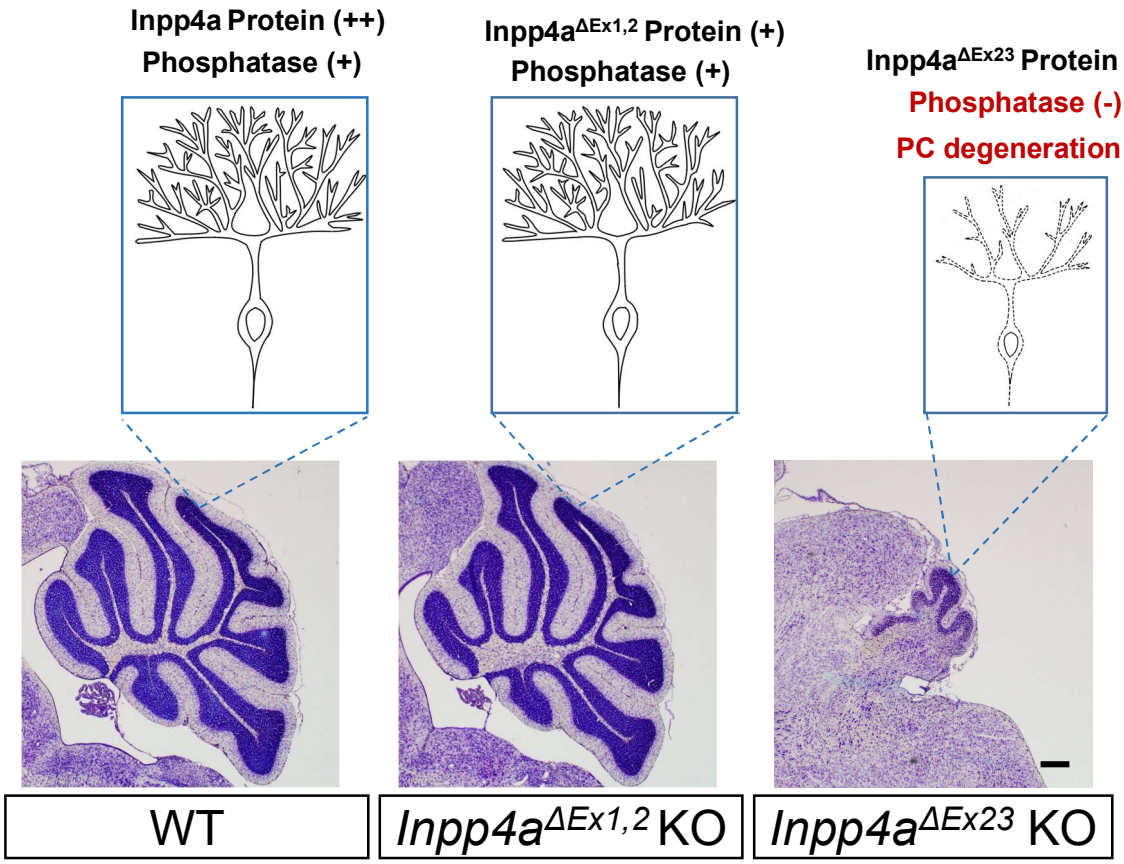

Tran et al., Figure 8